Advances in Aircraft and Spacecraft Science, *Vol. 13, No. 1 (2026) 17-44*
https://doi.org/10.12989/aas.2026.13.1.017

Techno-Press

Stability analysis of sandwich beams with functionally graded material skins and functionally graded porous core

Aissam Messaoudi[1a], Mourad Chitour[1b], Abdelhakim Bouhadra*[2,4], Abderrahmane Menasria[2,4c], Salah Refrafi[2d], Messaoud Bazzouzi[2,3e], Nabil Himeur[1,5f]

[1]*Department of Mechanical Engineering, Faculty of Sciences & Technology, University Abbes Laghrour, Khenchela 40000, Algeria*
[2]*Department of Civil Engineering, Faculty of Sciences & Technology, University Abbes Laghrour, Khenchela 40000, Algeria*
[3]*Civil Engineering Research Laboratory LRGC, Biskra University, 07000 Biskra, Algeria*
[4]*Materials and Hydrology Laboratory, University of Sidi Bel Abbes, Faculty of Technology, Algeria*
[5]*Laboratory of Engineering and Sciences of Advanced Materials (ISMA), Abbes Laghrour University Khenchela, 40004, Algeria*

(Received July 18, 2025, Revised September 25, 2025, Accepted November 26, 2025)

Abstract. This paper investigates the elastic instability behavior of sandwich beams featuring functionally graded skins and functionally graded porosity distribution of ceramic (Type-A) or metal (Type-B) core. Employing a high-order quasi-3D beam theory and the principle of virtual work, we derive the governing stability equations. The analysis considers three distinct porosity distributions (FGP) across the thickness, capturing variations in elastic modulus. The functionally graded porosity (FGP) distributions in functionally graded material (FGM) sandwich beams offer significant mechanical advantages over traditional porosity patterns. FGP facilitates the graded customization of stiffness, strength, and vibration response through the thickness, thereby optimizing weight and energy absorption while minimizing adverse effects, such as excessive deflection or diminished load capacity. This methodology enhances the overall structural performance and design. A parametric study evaluates how slenderness ratio, porosity volume fraction, aspect ratio, power-law grading index, and boundary conditions affect the critical buckling load (CBL). Numerical solutions are obtained and compared with existing higher-order shear deformation theories and full 2D/3D models, confirming the accuracy and robustness of the present approach.

Keywords: critical buckling load; elastic instability; functionally graded porosity (FGP); principle of virtual work; sandwich beams

*Corresponding author, Ph.D., E-mail: abdelhakim.bouhadra@univ-khenchela.dz
[a] Ph.D.
[b] Ph.D.
[c] Ph.D.
[d] Ph.D.
[e] Ph.D.
[f] Ph.D.

http://www.techno-press.org/aas/5
ISSN: 2287-528X (Print), 2287-5271 (Online)

1. Introduction

Functionally graded porous sandwich structures have garnered significant attention in modern engineering because of their exceptional mechanical properties, lightweight nature, and adaptability to multifunctional applications [1, 2]. These structures, characterized by spatially graded material properties and engineered porosity, exhibit unique responses to mechanical and thermal loads, necessitating advanced theoretical and computational frameworks for accurate analysis. Recent studies have demonstrated that porosity distribution, material gradation, and geometric nonlinearity significantly influence the buckling, free vibration, and static/dynamic behaviors [3, 4].

The buckling behavior of porous functionally graded (FG) sandwich beams and plates has been extensively investigated using higher-order theories and numerical methods in the literature. For instance, Akgöz et al. [5] employed the modified strain gradient theory to analyze axially FG microbeams, revealing the critical role of taper ratio and length scale parameters in buckling resistance. Similarly, Bridjesh et al. [6] highlighted the sensitivity of buckling loads to porosity distribution, showing that higher-order shear deformation theory (HSDT) provides more accurate predictions than classical beam theories. Chintalapudi et al. [4] further advanced reliability analysis by comparing Lagrangian, evolutionary, and GRG nonlinear methods, concluding that uniform porosity distributions enhance structural stability. Geetha et al. [7] proposed a higher-order shear deformation theory to examine the free vibrational response of functionally graded porous beams. Their findings indicated that porosity decreases natural frequencies and confirmed that higher-order theories outperform classical beam theories in predicting the vibrational characteristics.

Belarbi et al. [1] presented an advanced finite element model based on the first-order shear deformation theory to examine porous functionally graded plates with varying porosity distributions, proficient in accurately determining the bending, free vibration, and buckling responses under diverse loading conditions. This methodology is based on earlier research that acknowledged the significance of assessing the influence of porosity in structural analysis. Nguyen et al. [8] introduced a novel two-variable shear deformation theory that enhances the accuracy of predictions regarding bending, free vibration, and buckling responses in functionally graded porous beams, thereby offering improved forecasts relative to prior models while adequately accounting for porosity effects.

The Higher-order Shear Deformation Theory (HSDT) incorporating integral terms enhances the analysis of Functionally Graded Material (FGM) structures by refining the shear strain distributions across the thickness and eliminating the necessity for shear correction factors. This methodology employs undetermined integrals within the displacement fields to fulfill stress-free conditions, thereby improving the accuracy of the thermomechanical loading responses for thick structures. Chitour et al. [9] investigated the thermal buckling behavior of functionally graded (FG) sandwich plates subjected to varying temperature increases across their thickness and supported by a two-parameter elastic foundation. The mechanical properties of these FG sandwich plates are assumed to vary gradually through the thickness in accordance with a power law (P-FGM), as follows: Tamrabet et al. [10] examined the influence of porosity on the buckling behavior of thick functionally graded sandwich plates under various boundary conditions and subjected to different in-plane loads. This study formulates a newly developed sandwich plate utilizing a functionally graded material based on a modified power-law function, accommodating both symmetric and asymmetric configurations. Four distinct porosity distributions were

considered, varying according to the material property variations in the thickness direction of the face sheets of the sandwich plate. Additionally, metal foam was incorporated into the second model of the sandwich, which featured a metal foam core and functionally graded material face sheets. This investigation employs a novel quasi-three-dimensional high-shear deformation theory. Several recent studies on FGM beams have explored various materials, loading conditions, and boundary conditions [11-14].

Combined solicitations, such as thermo-mechanical buckling and coupled vibration-buckling responses, have been addressed using innovative modeling approaches. Van et al. [15] employed a phase-field model to analyze thermal buckling in cracked FG plates, emphasizing the stark contrast between temperature-dependent and temperature-independent material responses. Nguyen et al. [16] introduced a modified strain gradient theory for metal foam microbeams, capturing the size effects and predicting higher stiffness under combined loading. The multiscale framework proposed by Chen et al. [17] further validated the interplay between porosity and vibrational modes in FG beams, offering a unified approach for coupled analyses. Want et al. [18] proposed a high-order curved nanobeam model to analyze bending and buckling in functionally graded nanobeams with porosity. A two-phase local/nonlocal stress-driven gradient theory was proposed to capture the small-scale effects. The study revealed that the material gradient index and pore distribution pattern significantly influenced the dimensionless critical buckling loads. Microscale effects are significant in the analysis of porous functionally graded structures. Karamanli et al. [19] investigated the bending, vibration, and buckling of bi-directional functionally graded porous microbeams with varying material length scale parameters and demonstrated that the mechanical behavior was affected by both the material length scale parameter and porosity.

Recent advancements in computational techniques, such as artificial neural networks Turan et al. [3] and isogeometric analysis Khatir et al. [20], have further refined the predictions of buckling and vibration in porous FG structures. Adiyaman et al. [21] employed a novel method for the static analysis of two-dimensional functionally graded beams by incorporating an exponential function to represent the variation in material properties. The researchers performed parametric studies on the porosity effects, revealing that both porosity and its distribution significantly influenced the beam behavior. The broken-line hypothesis-based shear deformation beam theory (BSDBT) proposed by Wu et al. [22] demonstrated superior accuracy for porous beams, particularly at higher porosity coefficients. Meanwhile, Nguyen et al. [23] presented results of the Legendre-Ritz solution for free vibration and buckling of porous microbeams, offering explicit forms to predict mechanical behavior, which align well with existing solutions. Nguyen et al. [24] examined the Chebyshev polynomial-based Ritz solution for the thermal buckling and free vibration behaviors of metal foam beams. The Chebyshev method effectively predicted the critical buckling temperature and natural frequency across various boundary conditions and foam distributions.

Machine learning methodologies in artificial intelligence have begun to enhance traditional analytical methods in various ways. Tyran et al. [25] conducted comprehensive research on the free vibration and buckling of functionally graded porous beams using analytical methods, mathematical modeling, finite element analysis, and artificial neural networks. The results indicate that all three approaches produce comparable outcomes, highlighting the significant potential of the artificial neural network method in accurately predicting certain mechanical behaviors. Sandwich structures featuring porous cores represent a specialized research domain within functionally graded materials. Belarbi et al. [26] formulated an extended layerwise theory to analyze porous functionally graded sandwich plates, focusing on bending and free vibration. This theory incorporates various porosity distributions that significantly influence the mechanical

properties. Le and Nguyen [27] introduced a novel two-variable model that examined the vibration characteristics of porous functionally graded beams. The study demonstrated that the material characteristics, porosity, and boundary conditions significantly influenced the natural frequencies.

Advanced modeling has incorporated geometric features into the model, thereby fulfilling the design requirements. Gaspar et al. [28] examined the design of plane truss and frame-type structures made from functionally graded materials and proposed a novel method that characterizes these structures based on geometric features, such as height, rather than relying on the components of the material mixture gradient.

Recent studies have extensively investigated the mechanical behavior of porous and functionally graded (FG) structures under various loading and foundation conditions. Wave propagation in graphene platelet-reinforced FG porous plates on viscoelastic foundations has been examined by Gawah et al. [29] using an integral HSDT, while the bending response of porous FG plates under hygro-thermo-mechanical effects has been analyzed by Daouadji et al. [30]. Analytical approaches were also developed for imperfect FG beams on viscoelastic foundations [31] and for the thermal bending of porous cross-ply laminated plates using an improved FSDT [32]. Moreover, refined quasi-3D and size-dependent theories have been proposed for static and dynamic analyses of FG microplates with porosities [33], as well as for assessing the influence of porosity distribution on the buckling behavior of FG sandwich plates [34]. Several studies focused on porous FG nanocomposite beams and plates resting on viscoelastic foundations using finite element and higher-order shear deformation theories [35, 36] while others analyzed porosity-dependent wave propagation and vibration in FG-CNTRC beams [37, 38]. Novel formulations such as integral Timoshenko's theory and quasi-3D models were applied to explore free vibration, hygro-thermal effects, and bending of imperfect FG beams and sandwich plates [39]. Additional contributions examined static and dynamic responses of porous FG plates and shells using p-version finite element and quasi-3D HSDT approaches [40, 41]. Furthermore, the influence of porosity distributions on bending, buckling, and vibration of FG carbon nanotube-reinforced beams was highlighted [42] emphasizing the role of graded patterns, porosity types, and advanced foundation models in improving the accuracy of structural response predictions.

This study examines the buckling behavior of sandwich beams with functionally graded skins and functionally graded porosity (FGP) distributions subjected to mechanical loading under various boundary conditions. The novelty of this study lies in the implementation of a simplified quasi-3D higher-order shear deformation theory that utilizes only four variables through integral terms. Additionally, a novel functionally graded porosity (FGP) distribution for the ceramic (Type A) or metal (Type B) core was employed. Equilibrium equations were derived using the principle of virtual displacements, and solutions were provided for different boundary conditions. The accuracy of this formulation was validated by comparing the results with those of existing studies on similar problems. Furthermore, a parametric analysis elucidated the effects of key factors on the stability of sandwich beams incorporating isotropic cores with functionally graded porosity (FGP) and functionally graded material (FGM) face sheets.

2. Theoretical formulation

2.1 FG sandwich beams

An FGM sandwich beam with length a and rectangular cross-section of b × h (where h is the height and b is the width of the beam) is considered, as shown in Fig. 1.

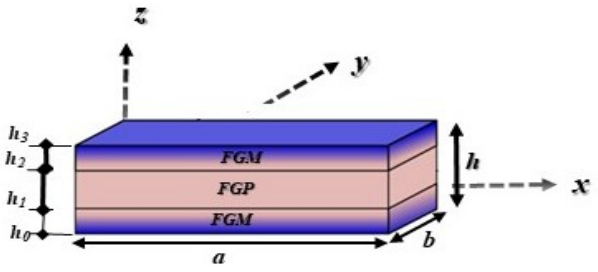

Figure 1. Geometry and coordinates of the FGM sandwich beams

The structure is composed of a mixture of isotropic ceramics and metal. The properties of these materials vary steadily with the volume fraction of the components in the thickness direction. For simplicity, the Poisson's ratio ν is assumed to be constant. Two different types of FGM sandwich beams, namely FGM-faces ceramic-core (model A) and FGM-faces metal-core (type B), are considered, as shown in Fig. 2.

Using the Voigt model material property in FGM, the material property of the elasticity modulus of the FG layers can be expressed in terms of the volume fractions of the ceramic and metal phases as follows

$$E^{(n)}(z) = (Ec - Em)V_c^{(n)} + Em, \tag{1}$$

Where *Ec* and *Em* are the properties of the ceramic and metal, respectively. *Vc* represents the volume fraction of the ceramic part, expressed as

Type A: sandwich beams with FG faces and ceramic core

$$\begin{aligned} V^{(1)} &= \left(\frac{z-h_0}{h_1-h_0}\right)^k \quad h_0 \le z \le h_1 \\ V^{(2)} &= 1 \qquad\qquad\quad h_1 \le z \le h_2 \\ V^{(3)} &= \left(\frac{z-h_3}{h_2-h_3}\right)^k \quad h_2 \le z \le h_3, \end{aligned} \tag{2}$$

Type B: sandwich beams with FG faces and metal core

$$\begin{aligned} V^{(1)} &= \left(\frac{z-h_1}{h_0-h_1}\right)^k h_0 \le z \le h_1 \\ V^{(2)} &= 0 h_1 \le z \le h_2 \\ V^{(3)} &= \left(\frac{z-h_2}{h_3-h_2}\right)^k h_2 \le z \le h_3, \end{aligned} \tag{3}$$

2.2 The mechanical properties of porous core

In this study, three typical porosity distribution Models of FGM sandwich beams, namely, uniform (D1), distribution stiffer at the surface of the core (D2), and distribution softer at the surface of the core (D3), were considered [11, 17, 54].

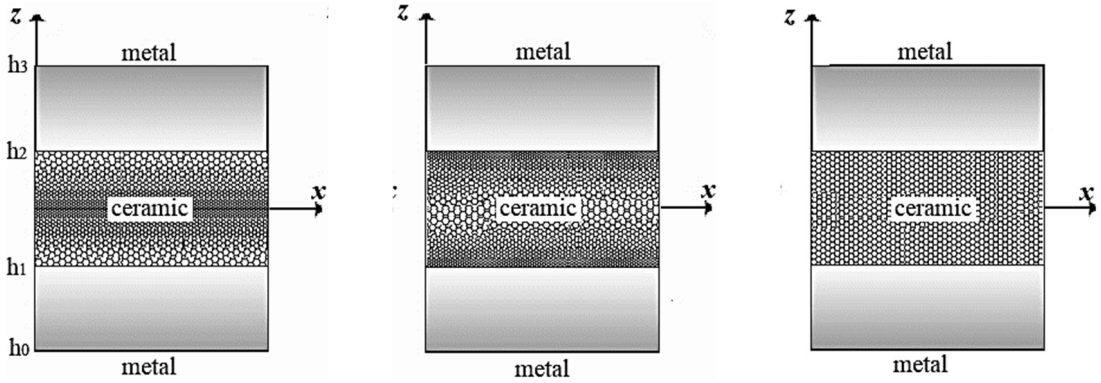

(a) Model 1 (D1) (b) Model 2 (D2) (c) Model 3 (D3)

Figure 2. (a) Different porosity distributions in the porous core of type-A beams (FG-faces, ceramic-core)

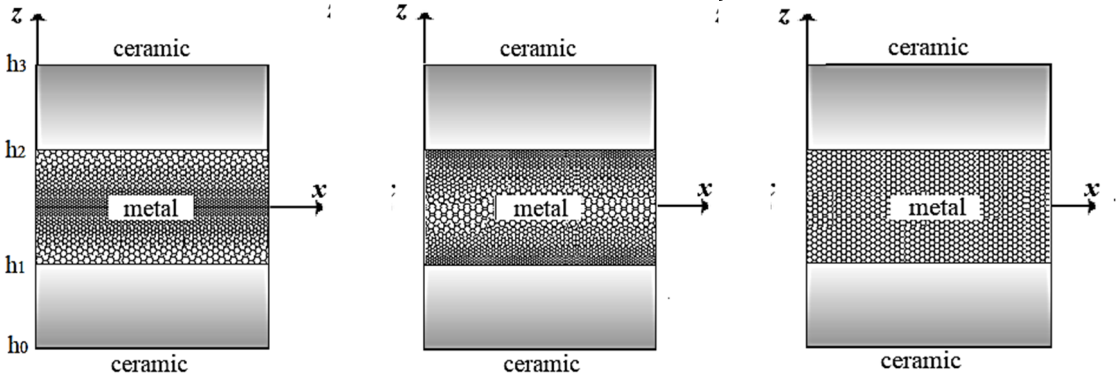

(a) Model 1 (D1) (b) Model 2 (D2) (c) Model 3 (D3)

Figure 2. (b) Different porosity distributions in the porous core of type-B beams (FG-faces, metal-core)

Model 1 (D1): Uniform porosity distribution type, Fig. 2(a).

$$E(z) = E_{core}\left(\frac{2}{\pi}\sqrt{1-\zeta} - \frac{2}{\pi} + 1\right)^2, \tag{4a}$$

$$\rho(z) = \rho_{core}\left(\frac{2}{\pi}\sqrt{1-\zeta} - \frac{2}{\pi} + 1\right), \tag{4b}$$

Model 2 (D2): The porosity distribution is stiffer at the surface beams, as shown in Fig. 2(b).

$$E(z) = E_{core}\left(1 - \zeta\, cos\left(\frac{\pi z}{h}\right)\right), \tag{5a}$$

$$\rho(z) = \rho_{core}\left(1 - \zeta_m\, cos\left(\frac{\pi z}{h}\right)\right), \tag{5b}$$

Model 3 (D3): The porosity distribution is softer at the surface beams, as shown in Fig. 2(c).

$$E(z) = E_{core}\left(1 - \zeta\, cos\left(\left|\frac{\pi z}{h}\right| - \frac{\pi}{2}\right)\right), \tag{6a}$$

$$E(z) = \rho_{core}\left(1 - \zeta_m\, cos\left(\left|\frac{\pi z}{h}\right| - \frac{\pi}{2}\right)\right), \tag{6b}$$

Where $\boldsymbol{E_{core}}$ is the Young's modulus, $\boldsymbol{\zeta}$ is the porosity parameter, and is the $\zeta_m = 1 - \sqrt{1-\zeta}$, mass density.

2.3 The mechanical properties of porous core

The stress-strain relations for the FGP beams are as follows

$$\begin{Bmatrix}\sigma_{xx}\\ \sigma_{zz}\\ \sigma_{xz}\end{Bmatrix}^{(n)} = \begin{bmatrix}Q_{11} & Q_{13} & 0\\ Q_{13} & Q_{33} & 0\\ 0 & 0 & Q_{55}\end{bmatrix}^{(n)} \begin{Bmatrix}\varepsilon_{xx}\\ \varepsilon_{yy}\\ \gamma_{xz}\end{Bmatrix}^{(n)}, \tag{7}$$

where

$$\begin{aligned} Q_{11}^{(n)} = Q_{33}^{(n)} &= \frac{E^{(n)}(z)}{(1-\nu^{(n)})^2}\\ Q_{13}^{(n)} &= \nu^{(n)} Q_{11}^{(n)}\\ Q_{55}^{(n)} &= \frac{E^{(n)}(z)}{2(1+\nu^{(n)})}, \end{aligned} \tag{8}$$

If the thickness stretching effect is omitted ($z = 0$), the elastic constants $Q_{ij}^{(n)}$ are reduced as follows

$$\begin{aligned} Q_{11}^{(n)} &= E^{(n)}(z)\\ Q_{13}^{(n)} &= 0\\ Q_{55}^{(n)} &= \frac{E^{(n)}(z)}{2(1+\nu^{(n)})}, \end{aligned} \tag{9}$$

2.4 Kinematics

The beam displacement field is given as follows, with the condition that the transverse shear stresses are zero at the top and bottom surfaces of the beams (z = ± h/2)

$$\begin{aligned} u(x,z) &= u_0(x) - z\frac{\partial w_0(x)}{\partial x} + K_1 f(z)\int \theta(x)dx\\ w(x,z) &= w_0(x) + g(z)\varphi_z(x), \end{aligned} \tag{10}$$

Where u_0, w_0, θ, and φ_z are unknown displacements of the mid-plane of the FG beam. The integral '$\int \theta dx$' used in Eq. (9) must be solved using the Navier procedure and is given as follows [11]

$$\int \theta(x)dx = A\frac{\delta\theta(x)}{\delta x}, \tag{11}$$

Where the coefficients A and K_1 are expressed as

$$K_1 = \lambda^2, A = -\frac{1}{\lambda^2}, \tag{12}$$

Alternatively

$$\lambda = \frac{m\pi}{a}, \tag{13}$$

The shape function (z) is assumed as

$$f(z) = (3/25)\pi z\left(\pi - \sqrt[3]{0.135}\, cosh(\pi z/h)\right), \tag{14}$$

Based on the small-strain elasticity theory, the strain expressions derived from the displacement field are given in Eq. (10) can be presented as follows

$$\begin{aligned} \varepsilon_{xx} &= \varepsilon_{xx}^0 + z\varepsilon_{xx}^1 + f(z)\varepsilon_{xx}^2 \\ \gamma_{zz} &= g'(z)\varepsilon_{zz}^0 \\ \gamma_{xz} &= \frac{\partial f(z)}{\partial z}\gamma_{xz}^0 = g(z)\gamma_{xz}^0, \end{aligned} \tag{15}$$

where $\varepsilon_{xx}^0, \varepsilon_{xx}^1, \varepsilon_{xx}^2, \varepsilon_{zz}^0$ and γ_{xz}^0 are related to the displacements *u, w,* θ_x and φ_z as follows

$$\begin{aligned} \begin{Bmatrix} \varepsilon_{xx}^0 \\ \varepsilon_{zz}^0 \end{Bmatrix} &= \begin{Bmatrix} \frac{\partial u_0}{\partial x} \\ \varphi_z \end{Bmatrix}, \begin{Bmatrix} \varepsilon_{xx}^1 \\ \varepsilon_{xx}^2 \end{Bmatrix} = \begin{Bmatrix} -\frac{\partial^2 w_0}{\partial x^2} \\ K_1 A \frac{\partial^2 \theta}{\partial x^2} \end{Bmatrix} \\ \{\gamma_{xz}^0\} &= \left\{k_1 A \frac{\partial \theta}{\partial x} + \frac{\partial \varphi_z}{\partial x}\right\}, \end{aligned} \tag{16}$$

2.5 Variational formulation

Using the principle of virtual work, the governing stability equations for the FG sandwich beams are obtained as follows

$$\Pi = U + V, \tag{17}$$

where *u* and *v* are the strain energy and work done, respectively. The variation of the strain energy can be stated as

$$\begin{aligned} \delta U &= \frac{1}{2}\int_0^a \int_0^b \left[\sum_{n=1}^{3} \int_{h_n-1}^{h_n} \begin{pmatrix} \sigma_{xx}\delta\varepsilon_{xx} + \\ \sigma_{zz}\delta\varepsilon_{zz} + \\ \tau_{xz}\delta\gamma_{xz} \end{pmatrix} dz\right] dydx \\ &= \int_0^a \begin{pmatrix} N_{xx}\delta\varepsilon_{xx}^0 + M_{xx}\delta\varepsilon_{xx}^1 \\ +P_{xx}\delta\varepsilon_{xx}^2 + N_{zz}\delta\varepsilon_{zz}^0 + \\ S_{xz}\delta\gamma_{xz}^0 \end{pmatrix} dx, \end{aligned} \tag{18}$$

Also, the variation of potential energy of the applied external loads (N_0) is expressed as

$$\delta V = -\frac{1}{2}\int_{-a/2}^{a/2} N_0 \left(\frac{\partial w}{\partial x}\right)^2 dx, \tag{19}$$

Where N_{xx}; N_{zz}, M_{xx}; P_{xx}, and S_{xz} are the stress resultants, defined as

$$\begin{aligned} N_{xx} &= \sum_{n=1}^{3} \int_{h_{n-1}}^{h_n} \sigma_{xx} dz\,, M_{xx} = \sum_{n=1}^{3} \int_{h_{n-1}}^{h_n} \sigma_{xx} z dz \\ P_{xx} &= \sum_{n=1}^{3} \int_{h_{n-1}}^{h_n} \sigma_{xx} f(z) dz\,, N_{zz} = \sum_{n=1}^{3} \int_{h_{n-1}}^{h_n} \sigma_{zz} g'(z) dz \\ S_{xz} &= \sum_{n=1}^{3} \int_{h_{n-1}}^{h_n} \tau_{xz} g(z) dz\,, \end{aligned} \tag{20}$$

Table 1. The admissible functions *Xm, Yn*

boundary conditions	The functions X_m and Y_m	
	X_m	Y_m
simply-supported (S-S)	Sin(λx)	Sin(λx)
clamped-clamped (C-C)	Sin(λx) Cos(λx)	Sin(λx)

By substituting Eqs. (7) and (15) into Eq. (20), the stress resultants can be expressed in terms of displacements as follows

$$\begin{Bmatrix} N_{xx} \\ M_{xx} \\ P_{xx} \\ N_{zz} \end{Bmatrix} = \begin{bmatrix} A_{11} & B_{11} & Bs_{11} & L_{11} \\ & D_{11} & Ds_{11} & L_{22} \\ & & Hs_{11} & L_{33} \\ Sym & & & L_{44} \end{bmatrix} \begin{bmatrix} \varepsilon_{xx}^{0} \\ \varepsilon_{xx}^{1} \\ \varepsilon_{xx}^{2} \\ \varepsilon_{zz}^{0} \end{bmatrix} \tag{21}$$
$$\{S_{xz}\} = [Fs_{55}]\{\gamma_{xz}^{0}\},$$

Where

$$A_{11} = \sum_{n=1}^{3} \int_{h_n-1}^{h_n} Q_{11}^{(n)}\, dz,\ B_{11} = \sum_{n=1}^{3} \int_{h_n-1}^{h_n} Q_{11}^{(n)} z\, dz,\ D_{11} = \sum_{n=1}^{3} \int_{h_n-1}^{h_n} Q_{11}^{(n)} z^2\, dz,$$
$$Bs_{11} = \sum_{n=1}^{3} \int_{h_n-1}^{h_n} Q_{11}^{(n)} f(z)\, dz,\ Ds_{11} = \sum_{n=1}^{3} \int_{h_n-1}^{h_n} Q_{11}^{(n)} z\, f(z) dz, \tag{22}$$
$$L_{11} = \sum_{n=1}^{3} \int_{h_n-1}^{h_n} Q_{13}^{(n)}\, g'(z) dz,\ L_{22} = \sum_{n=1}^{3} \int_{h_n-1}^{h_n} Q_{13}^{(n)} z g'(z)\, dz,$$
$$L_{33} = \sum_{n=1}^{3} \int_{h_n-1}^{h_n} Q_{13}^{(n)} f(z) g'(z) dz,\ L_{44} = \sum_{n=1}^{3} \int_{h_n-1}^{h_n} Q_{13}^{(n)} g'(z)^2\, dz,$$
$$Fs_{44} = \sum_{n=1}^{3} \int_{h_n-1}^{h_n} C_{55}^{(n)} g(z)^2\, dz\ ,$$

2.5 Governing equations

By integrating Eq. (19) and (18) by parts and collecting the coefficients of δu, δw, $\delta\theta_x$, and $\delta\varphi_z$, the governing equations of equilibrium can be further written as

$$\begin{aligned} \delta u_0 &: -\frac{\partial N_{xx}}{\partial x} = 0 \\ \delta w_0 &: -\frac{\partial^2 M_{xx}}{\partial x^2} + N_0 \frac{\partial^2 w}{\partial x^2} = 0 \\ \delta\theta &: K_1 A \frac{\partial^2 P_{xx}}{\partial x^2} - K_1 A \frac{\partial S_{xz}}{\partial x} = 0 \\ \delta\varphi_z &: N_{zz} - \frac{\partial S_{xz}}{\partial x} = 0\ , \end{aligned} \tag{21}$$

Substituting Eqs. (16), (20), and (21) into Eq. (23), the governing equations of equilibrium are defined by

$$\begin{aligned} \delta u_0 &: A_{11} \frac{\partial^2 u_0}{\partial x^2} + B_{11} \frac{\partial^3 w_0}{\partial x^3} - K_1 A B s_{11} \frac{\partial^3 \theta}{\partial x^3} - L \frac{\partial \varphi_z}{\partial x} = 0 \\ \delta w_0 &: -Bs_{11} \frac{\partial^3 u_0}{\partial x^3} + D_{11} \frac{\partial^4 w_0}{\partial x^4} - Ds_{11} K_1 A \frac{\partial^4 \theta}{\partial x^4} - La \frac{\partial^2 \varphi_z}{\partial x^2} + N_0 \frac{\partial^2 w_0}{\partial x^2} = 0 \\ \delta\theta &: -Bs_{11} K_1 A \frac{\partial^3 u_0}{\partial x^3} + Ds_{11} K_1 A \frac{\partial^4 w_0}{\partial x^4} - (K_1 A)^2 (Hs_{11} \frac{\partial^4 \theta}{\partial x^4} - Fs_{44} \frac{\partial^2 \theta}{\partial y^2}) + (K_1 A)(R - Fs_{44}) \frac{\partial^2 \varphi_z}{\partial x^2} = 0 \end{aligned} \tag{24}$$

$$\delta\varphi_z: L\frac{\partial u_0}{\partial x} - La\frac{\partial^2 w_0}{\partial x^2} + K_1 A\frac{\partial^2 \theta}{\partial x^2}(R - Fs_{44}) + Ra\varphi_z - Fs_{44}\frac{\partial^2 \varphi_z}{\partial x^2} = 0\ ,$$

The exact solution of Eqs. (24) For FG beams under various boundary conditions, the corresponding equations can be derived. The functions corresponding to different boundary conditions (supported - SS and clamped edge - CC) are listed in Table 1.

$$\begin{Bmatrix} u_0(x) \\ w_0(x) \\ \theta(x) \\ \varphi_z(x) \end{Bmatrix} = \begin{Bmatrix} U_m \frac{\partial X_m}{\partial x} Y_m \\ W_m X_m Y_m \\ \theta_m X_m Y_m \\ \psi_m X_m Y_m \end{Bmatrix}, \tag{25}$$

U_m, W_m, θ_m, and ψm denote arbitrary parameters. Substituting expressions (25) into the governing Eqs. (24), one obtains, after some mathematical manipulations, the following equations

$$[S]\{\Delta\} = \{0\}, \tag{26}$$

where

$$\{\Delta\} = \{U_m, W_m, \theta_m, \psi_m\}^T, \tag{27}$$

Where the components of the stiffness matrix [S] are defined by

$$[S] = \begin{bmatrix} S_{11} & S_{12} & S_{13} & S_{14} \\ S_{21} & S_{22} + Ncr & S_{23} & S_{24} \\ S_{31} & S_{32} & S_{33} & S_{34} \\ S_{41} & S_{42} & S_{43} & S_{44} \end{bmatrix}, \tag{28}$$

where the critical buckling load is given by

$$Ncr = N_0\alpha_9, \tag{29}$$

in which

$$\begin{aligned} S_{11} &= -A_{11}\alpha_{12} & S_{21} &= -B_{11}\alpha_{13} \\ S_{12} &= B_{11}\alpha_{12} & S_{22} &= D_{11}\alpha_{13} \\ S_{13} &= -Bs_{11}\alpha_{12}k_1 A & S_{23} &= -Ds_{11}k_1 A\alpha_{13} \\ S_{14} &= -L\alpha_6 & S_{24} &= -La\alpha_9 \\ S_{31} &= Bs_{11}k_1 A\alpha_{13} & S_{41} &= L\alpha_9 \\ S_{32} &= -Ds_{11}k_1 A\alpha_{13} & S_{42} &= -La\alpha_9 \\ S_{33} &= (k_1 A)^2(Hs_{11}\alpha_{13} - Fs_{44}\alpha_9) & S_{43} &= K_1 A\alpha_9(R - Fs_{44}) \\ S_{34} &= K_1 A\alpha_9(R - Fs_{44}) & S_{44} &= Ra\alpha_1 - Fs_{44}\alpha_9 \end{aligned}, \tag{30}$$

with

$$\begin{aligned} (\alpha_1) &= \int_0^b \int_0^l (X_m Y_m) X_m Y_m dxdy, \\ (\alpha_6, \alpha_{12}) &= \int_0^b \int_0^l (X'_m Y_m, X'''_m Y_m) X'_m Y_m \ dxdy, \quad b = 1, \\ (\alpha_9, \alpha_{11}, \alpha_{13}) &= \int_0^b \int_0^l (X''_m Y_m, X''_m Y''_m, \\ &\quad X''''_m Y_m) X_m Y_m \ dxdy, \end{aligned} \tag{31}$$

3. Numerical results and discussion

The analysis focuses on the buckling behavior of FG beams under various boundary conditions, encompassing different types of sandwich beams and porosity models. Multiple parametric studies were conducted, and the obtained solutions were compared with existing data from the literature. The FGM investigated in this study consisted of a composite blend comprising alumina (Al2O3) as the ceramic phase and aluminum (Al) as the metal phase. The mechanical properties, including the Young's modulus and Poisson's ratio, are listed in Table 2. To facilitate the analysis, all the results were expressed in non-dimensional terms. This allows for a more convenient comparison and understanding of the results. The analysis focuses on the buckling behavior of FG beams under various boundary conditions, encompassing different types of sandwich beams and porosity models. Multiple parametric studies were conducted, and the obtained solutions were compared with existing data from the literature. The FGM investigated in this study consisted of a composite blend comprising alumina (Al2O3) as the ceramic phase and aluminum (Al) as the metal phase. The mechanical properties, including the Young's modulus and Poisson's ratio, are listed in Table 1. To facilitate the analysis, all the results were expressed in non-dimensional terms. This allows for a more convenient comparison and understanding of the results.

Table 3 presents a comprehensive comparison of the non-dimensional critical buckling loads for functionally graded material (FGM) beams, accounting for geometric imperfections across various length-to-height ratios and boundary conditions. This table examines two types of imperfect beams (Imperfect I and Imperfect II) with $\zeta = 0.5$, indicating a moderate variation in the material properties across the thickness of the beams. The examined length-to-height ratios were 10, 20, and 50. Two boundary conditions were studied: SS and CC. The comparisons encompass various theoretical studies that calculate critical buckling loads, including those by Nguyen et al. [8], who considered both shear deformation effects and their exclusion, as well as the contributions from [43, 44].

Specific notable trends can be observed from these data. CC beams demonstrated considerably greater critical buckling loads than SS beams, practically four times greater, which can be expected owing to the added constraint. As the l/h ratio increases and the beams become slender, the critical buckling loads decrease considerably. For example, in the SS Imperfect I-beams, the critical buckling load decreases from 0.010615 (l/h = 10) to 0.000435 (l/h = 50). The Imperfect II beams consistently predicted greater essential loads owing to buckling than the Imperperfect I beams, indicating that different imperfection geometries or equivalent imperfections lead to varying structural stabilities.

The inclusion of shear deformation (Nguyen et al. [8] with shear) purportedly lowers the critical buckling load compared to classical beam theory, with this effect being particularly pronounced in thick beams (l/h = 10). The results of the present study concur with those of other studies, as the values for all cases tended to fall between the values predicted by other studies, thus confirming the validity of the present investigation.

Table 2. Material properties used in the FG Beams

Properties	Alumina (Al2O3)	Aluminum (Al)
Young's modulus E (GPa)	380	70
Poisson's ratio ν	0.3	0.3

Table 3. Non-dimensional critical buckling load of Imperfect I and Imperfect II beams (ζ= 0.5) with different BCs and l/h ratios

BC	Theory	Imperfect I			Imperfect II		
		10	20	50	10	20	50
SS	Nguyen et al. [8] (No shear)	0.010887	0.002722	0.000435	0.013474	0.003368	0.000539
	Nguyen et al. [8] (shear)	0.010574	0.002702	0.000435	0.012953	0.003335	0.000538
	Chen et al. [43]	/	/	/	/	0.003338	/
	Jamshidi et al. [44]	/	/	/	/	0.003339	/
	Present	0.010615	0.002704	0.000435	0.013025	0.003339	0.000538
CC	Nguyen et al. [8] (No shear)	0.043548	0.010887	0.001742	0.053895	0.013474	0.002156
	Nguyen et al. [8] (shear)	0.038942	0.010574	0.001734	0.046433	0.012953	0.002142
	Chen et al. [43]	/	/	/	/	0.013010	/
	Jamshidi et al. [44]	/	/	/	/	0.013010	/
	Present	0.039505	0.010645	0.001735	0.047374	0.013025	0.002144

As the porosity coefficient (ζ) increases from 0.2 to 0.8, the non-dimensional critical buckling load for the (SS) and (CC) beams decreases. The results are presented in Table 4. This decrease occurs because a higher porosity makes the functionally graded material (FGM) less stiff, which means that the beam is less able to resist buckling when subjected to compressive loads.

At ζ = 0.2, the buckling load for CC beams (139.011) is approximately 291% higher than that for SS beams (35.518) for Imperfect I. This significant difference is due to the CC boundary conditions, which prevent rotation at both ends, thereby making the structure more rigid and

Table 4. Non-dimensional critical buckling load (x10− 4) of beams with different BCs and porosity coefficient, l/h =20

BC	Theory		ζ			
			0.2	0.4	0.6	0.8
SS	Nguyen et al. [8]	Imperfect I	35.518	29.946	23.953	17.146
	Present		35.581	29.999	23.995	17.175
	Nguyen et al. [8]	Imperfect II	37.839	34.849	31.842	28.793
	Present		37.919	34.942	31.961	28.971
	Nguyen et al. [8]	Imperfect III	33.629	26.432	19.226	12.009
	Present		33.678	26.461	19.240	12.014
CC	Nguyen et al. [8]	Imperfect I	139.011	117.203	93.746	67.103
	Present		139.967	118.009	94.3908	67.5648
	Nguyen et al. [8]	Imperfect II	147.778	135.665	123.300	110.322
	Present		148.992	137.078	125.094	112.980
	Nguyen et al. [8]	Imperfect III	131.872	103.892	75.792	47.520
	Present		132.619	104.343	76.014	47.597

Table 5 Nondimensional critical buckling loads of S-S FGM sandwich beams of type A for L/h = 5

k	theory	Scheme				
		1-0-1	1-1-1	2-1-2	1-8-1	1-2-1
0	Nguyen et al. [45]	48.5964	48.5964	48.5964	--	48.5964
	Liu et al. [47]	48.7271	48.8107	48.7322	49.1309	48.9108
	Vo et al. [46] $\varepsilon_z \neq 0$	49.5906	49.5906	49.5906	49.5906	49.5906
	Present $\varepsilon_z = 0$	48.6043	48.6043	48.6043	48.6043	48.6043
	Present $\varepsilon_z \neq 0$	49.6477	49.6477	49.6477	49.6477	49.6477
0.5	Nguyen et al. [45]	27.8380	31.8650	30.0146	--	34.7546
	Liu et al. [47]	27.3096	31.6663	29.3256	42.3053	34.6366
	Vo et al. [46] $\varepsilon_z \neq 0$	28.4624	32.5699	30.6825	42.8751	35.5156
	Present $\varepsilon_z = 0$	27.8525	31.8796	30.0272	42.0085	34.7743
	Present $\varepsilon_z \neq 0$	28.5125	32.6351	30.7399	42.9569	35.5920
1	Nguyen et al. [45]	19.6541	24.5602	22.2121	--	28.4440
	Liu et al. [47]	19.8582	24.7869	22.1799	39.2569	28.7246
	Vo et al. [46] $\varepsilon_z \neq 0$	20.7425	25.1075	22.7065	39.6144	29.0755
	Present $\varepsilon_z = 0$	19.6444	24.5576	22.2044	38.8061	28.4519
	Present $\varepsilon_z \neq 0$	20.1289	25.1693	22.7569	39.7052	29.1540
2	Nguyen et al. [45]	13.5820	18.3596	15.9167	--	22.7859
	Liu et al. [47]	13.7865	18.6296	15.9109	36.1811	23.1100
	Vo et al. [46] $\varepsilon_z \neq 0$	13.8839	18.7772	16.2761	36.4677	23.3042
	Present $\varepsilon_z = 0$	13.5692	18.3536	15.9061	35.7157	22.7904
	Present $\varepsilon_z \neq 0$	13.9072	18.8299	16.3139	36.5652	23.3792
5	Nguyen et al. [45]	10.1488	13.7226	11.6697	--	18.0915
	Liu et al. [47]	10.1651	13.9266	11.6064	33.2846	18.4096
	Vo et al. [46] $\varepsilon_z \neq 0$	10.3673	14.0353	11.9301	33.4958	18.5092
	Present $\varepsilon_z = 0$	10.1315	13.7128	11.6556	32.7972	18.0911
	Present $\varepsilon_z \neq 0$	10.3698	14.0719	11.9482	33.5972	18.5748
10	Nguyen et al. [45]	9.4543	12.2621	10.5370	--	16.3789
	Liu et al. [47]	9.3964	12.4551	10.4601	32.1157	16.7535
	Vo et al. [46] $\varepsilon_z \neq 0$	9.6535	12.5393	10.7689	32.2264	16.7574
	Present $\varepsilon_z = 0$	9.4360	12.2503	10.5209	31.7776	16.3816
	Present $\varepsilon_z \neq 0$	9.6494	12.5664	10.7769	32.8911	16.8173

capable of supporting a greater weight. SS beams, on the other hand, only stop translational movement. The buckling load decreases at different rates for different types of imperfections as ζ increases.

• Imperfect I decreases by an average of 6 units for every 0.2 increase in ζ (for example, SS goes from 35.518 to 17.146 (52% reduction) and CC goes from 139.967 to 67.565 (52%

reduction)). This sharp drop suggests that the porosity is evenly or symmetrically distributed, which makes the beam cross-section less stiff.

• Imperfect II decreases by an average of three units for every 0.2 increase (for example, SS goes from 37.839 to 28.793 (a 24% decrease), and CC goes from 148.992 to 112.980 (a 24% decrease). The less severe drop suggests that the porosity distribution is not linear or is graded, indicating that the material remains somewhat stiff because the effects of porosity are not uniform.

• Imperfect III decreases by an average of seven units for every 0.2 increase (for example, SS: 33.629 to 12.009 (64% decrease) and CC from 132.619 to 47.597 (64% decrease)). This sharp drop indicates that the porosity is highly localized or uneven, creating weak spots that significantly compromise the strength of the structure.

The results in Table 5 show how the non-dimensional critical buckling load changes for SS FGM sandwich beams with different power-law indices (k) and layer schemes. The results show that considering the transverse normal strain ($\varepsilon z \neq 0$) always leads to higher critical buckling loads than ignoring this effect ($\varepsilon z = 0$) for all configurations.

The current study finds that the buckling loads are 48.6043 when $\varepsilon z = 0$ and 49.6477 when $\varepsilon z \neq 0$ for the homogeneous case ($k = 0$). This was a 2.1% increase. As the material gradient parameter k increases, this improvement becomes more significant. This implies that the effects of the transverse normal strain become more significant in highly graded materials, where variations in properties through the thickness of the material lead to considerable coupling between in-plane and out-of-plane deformations.

The 1-8-1 scheme always yields the highest critical buckling loads for all material gradient parameters. For example, it yields a value of 42.9569 for $k = 0.5$ with $\varepsilon z \neq 0$, whereas the 1-0-1 configuration only yields 28.5125. The thick core in the 1-8-1 scheme significantly increased the second moment of area, making it more resistant to bending-induced buckling. This explains the significant difference. Even though the core material is softer than the face sheets, it makes the structure significantly stiffer when it is thick enough.

As the material gradient parameter k increased from 0 to 10, all configurations exhibited a steady decrease in buckling resistance. However, the degradation patterns differed significantly for each scheme. When transitioning from a fully ceramic beam ($k = 0$) to one with some metal content ($k = 0.5$), the buckling load decreased by 42.6% in the 1-0-1 configuration. This significant drop demonstrates that even a small amount of metal can significantly reduce the stiffness. The cuts decrease as (k) increases: 29.4% from k=0.5 to 1, 30.9% from k=1 to 2, 25.4% from k=2 to 5, and only 6.9% from k=5 to 10. This pattern shows that the beam is less sensitive to changes in k when the metal phase is charged.

In contrast, the 1-8-1 scheme, which features a thick ceramic core, exhibits significantly fewer drops in the buckling load as k increases. The most significant drop is 13.5% from k=0 to 0.5, and then the changes get smaller: 7.6% from k=0.5 to 1, 7.9% from k=1 to 2, 8.1% from k=2 to 5, and 2.1% from k=5 to 10. This demonstrates how the ceramic core maintains its stiffness, even as the metal phase becomes more significant.

The fact that the buckling loads decrease as the k parameter increases demonstrates the variation in the FGM properties. Higher k values typically indicate that the material properties change more significantly, which can create weak points in the structure. In power-law FGMs, increasing k usually means going from compositions rich in ceramics to compositions rich in metals. The metal phase typically has a lower elastic modulus, which makes the entire structure less stiff and less able to resist buckling than the ceramic phase.

Table 6. Nondimensional critical buckling load of S-S FGM sandwich beams with type A for l/h = 20

k	theory	Scheme				
		1-0-1	1-1-1	2-1-2	1-8-1	1-2-1
0	Nguyen et al. [45]	53.2364	53.2364	53.2364	--	53.2364
	Liu et al. [47]	53.2494	53.2552	53.2488	53.2847	53.2641
	Vo et al. [46] $\varepsilon_z \neq 0$	53.3145	53.3145	53.3145	53.3145	53.3145
	Present $\varepsilon_z = 0$	53.2372	53.2372	53.2372	53.2372	53.2372
	Present $\varepsilon_z \neq 0$	53.4236	53.4236	53.4236	53.4236	53.4236
0.5	Nguyen et al. [45]	29.6965	34.0722	32.0368	--	37.3054
	Liu et al. [47]	29.0150	33.7947	31.3856	45.4175	37.1583
	Vo et al. [46] $\varepsilon_z \neq 0$	29.7626	34.1380	32.1022	45.6424	41.8227
	Present $\varepsilon_z = 0$	29.7172	34.0864	32.0533	45.5756	37.3165
	Present $\varepsilon_z \neq 0$	29.8283	34.2132	32.1731	45.7331	37.4532
1	Nguyen et al. [45]	20.7213	25.9588	23.4212	--	30.2306
	Liu et al. [47]	20.8953	26.0698	23.4029	41.9519	30.3118
	Vo et al. [46] $\varepsilon_z \neq 0$	20.7530	25.9989	23.4572	41.9639	30.2774
	Present $\varepsilon_z = 0$	20.7206	25.9588	23.4208	41.9021	30.2312
	Present $\varepsilon_z \neq 0$	20.8021	26.0599	23.5128	42.0449	30.3451
2	Nguyen et al. [45]	14.1974	19.2000	16.6051	--	23.9899
	Liu et al. [47]	14.4247	19.4000	16.6391	38.4860	24.1595
	Vo et al. [46] $\varepsilon_z \neq 0$	14.2190	19.2299	16.6307	38.4419	24.0276
	Present $\varepsilon_z = 0$	14.1966	19.1996	16.6044	38.3849	23.9903
	Present $\varepsilon_z \neq 0$	14.2560	19.2812	16.6756	38.5139	24.0860
5	Nguyen et al. [45]	10.6176	14.2285	12.0886	--	18.8874
	Liu et al. [47]	10.7278	14.4290	12.0566	35.2493	19.1031
	Vo et al. [46] $\varepsilon_z \neq 0$	10.6330	14.2505	12.1068	35.1400	18.9172
	Present $\varepsilon_z = 0$	10.6162	14.2278	12.0875	35.0875	18.8873
	Present $\varepsilon_z \neq 0$	10.6578	14.2946	12.1412	35.2048	18.9715
10	Nguyen et al. [45]	9.9850	12.6820	10.9075	--	17.0445
	Liu et al. [47]	10.0445	12.9274	10.9425	33.9515	17.3560
	Vo et al. [46] $\varepsilon_z \neq 0$	9.9995	12.7014	10.9239	33.7367	17.0712
	Present $\varepsilon_z = 0$	9.98365	12.6812	10.9066	33.9917	17.0444
	Present $\varepsilon_z \neq 0$	10.0199	12.7408	10.9523	33.8811	17.1193

Various sandwich schemes provide important insights into the design of FGM structures. The 2-1-2 configuration exhibited moderate performance by balancing the thickness of the face sheet with the presence of the core. The 1-2-1 scheme, on the other hand, offers good buckling resistance by optimizing the ratio of face to core. The 1-1-1 scheme is a balanced approach, but it does not achieve the same level of performance as either thin-faced or thick-cored designs.

The validation against reference studies shows that the current εz = 0 results are very similar to the [45], and the (εz ≠ 0) results are very similar to what [46] theory says will happen.

Slight differences of 0.1–0.5% typically occur owing to variations in the implementation of numbers, mesh refinement, or the definition of convergence. The results of this study (εz ≠ 0) are always between Nguyen et al. [45] and Vo et al. [46].

The findings presented in Table 6 indicate that the behaviors of thin (***l*/*h*** = 20) and thick (l/h = 5) beams differ significantly. For thin beams, the transverse normal strain effect ($\varepsilon z \neq 0$) results in much smaller increases in buckling resistance, usually between 0.3% and 0.4%, as opposed to the 2-3% seen in thick beams (***l*/*h*** = 5). This is because bending deformation is the primary effect of classical Euler buckling behavior in thin beams, with transverse normal strain effects playing a secondary role. The through-thickness stress variations that drive the three-dimensional coupling effects are less significant owing to the geometric slenderness of the structure.

All configurations exhibited systematic reductions in buckling resistance as the material gradient parameter k increased from 0 to 10, although the degradation patterns differed significantly between the schemes. When switching from a pure ceramic (k=0) to a slight metal mixture (k=0.5), the 1-0-1 configuration suffers the most drastic reduction in buckling strength, with a 44.2% decrease. This demonstrates the sensitivity of these beams to minute metal particles. As k rises further, the reductions decrease: 30.3% from k = 0.5 to 1, 31.5% from k = 1 to 2, 25.2% from k = 2 to 5, and only 6.9% from k = 5 to 10. According to this analysis, the most substantial degradation occurs in the early phases of material grading (k = 0 to k = 1), with diminishing effects at higher k values as the material approaches its fully metal-rich state.

Even though the 1-8-1 scheme exhibits a more moderate decline between k=0 and 0.5, the effects of increasing k further decrease to 8.1% (0.5 to 1), 8.4% (1 to 2), 8.6% (2 to 5), and only 3.8% (5 to 10). This illustrates how the 1-8-1 design's thick ceramic core contributes to stability, even when additional metal is added.

The various sandwich schemes provide important design insights for FGM structures. While the 1-2-1 scheme offers good buckling resistance through optimized face-to-core ratios, the 2-1-2 configuration balances the face sheet thickness and core presence to provide moderate performance. Although the 1-1-1 scheme is a balanced approach, it falls short of both thin-faced and thick-cored designs in terms of their performance.

The behavior of FGM sandwiches differs fundamentally when comparing thick (***l*/*h*** = 5) and slender (***l*/*h*** = 20) beams. With increasing material gradients, thinner beams exhibit more predictable degradation patterns, lower sensitivity to transverse strain effects, and fewer benefits from thick-core configurations. Because the shear deformation effects that benefit from the core thickness are subordinated to the classical bending theory, the thick-core advantage is diminished in thin beams.

With the current εz = 0 results closely matching Nguyen et al. [45] values and the (εz ≠ 0) results well aligned with Vo et al. [46] theory predictions, the validation against reference studies demonstrates excellent agreement. Differences in mesh refinement, convergence criteria, or numerical implementation are usually the cause of minor discrepancies of 0.1-0.5%. The results of the current study (εz ≠ 0) consistently fall between the full model. Vo et al. [46] and Nguyen et al. [45] predictions.

In Table 7, the results show that the boundary conditions of clamped-clamped produce much higher critical buckling loads than simply supported, with values approximately 3.0-3.2 times higher across all cases. For the homogeneous case (k = 0) with $\varepsilon z \neq 0$, the present study yielded 160.0357 for CC beams compared with 49.6477 for SS beams from Table 5. The clamped ends

provide full rotational restraint at both ends of the beam, resulting in significantly higher flexural rigidity than that of simply supported beams, which prevents buckling modes. With fixed boundary conditions, the rotational degrees of freedom in the first buckling mode are completely restricted, resulting in higher-order modes that require significantly more energy to excite.

The effect of the transverse normal strain ($\varepsilon z \neq 0$) added significant improvements to the buckling resistance in thick clamped beams in the typical 5-6% improvement range compared with the classical formulation ($\varepsilon z = 0$). The results related to the buckling of (CC) FGM sandwich beams of Type A configuration at a length-to-height ratio of $l/h = 5$ are presented. For the first scheme, 1-0-1, there is an observed decrease of 42.3% in buckling load when moving from pure ceramics (k=0, 160.0357) to a mixture of metal (k=0.5, 92.3501). The transition from $k = 0.5$ to 1, from $k = 1$ to 2, and from $k = 2$ to 5 illustrated reductions of 27.1%, 29.3%, and 25.8%, respectively. There was a more modest reduction of 9.5% for k=5–10. The metal weakens the buckling stability of the beam as the metal increases, although the reduction in the buckling load decreases with k. Examining the 1-8-1 scheme, we observed a distinct trend, with a reduction of only 11.4% when transitioning from $k = 0$ to 0.5 (160.0357 to 141.8621). Then, moving from $k = 0.5$ to 1, 1 to 2, 2 to 5, and 5 to 10, we observed even lower reductions of 6.4%, 6.8%, 7.0%, and 3.0%, respectively. Based on the changes observed in the k values, we can confidently assert that the 1-8-1 configuration has better stability than the configuration with a nearly ceramic center. In particular, when a thicker ceramic is used, as found in 1-8-1, the stability and structural integrity of the beam are maintained even when there is an abundance of metal complicating the beam structure.

There are several key points evident from our analysis.

1. For $k > 1$, the 1-8-1 configuration provided a larger buckling load than when both ends of the baton were of a metal configuration (one being a metal core); it was, on average, 3.5 times larger when $k = 10$.
2. Both schemes indicate that the most stiffness loss occurs in the lower k range (0-2), whereas dimensionless returns are observed for higher values.
3. The results of the Present study, with ($\varepsilon z \neq 0$), are generally in agreement and slightly exceed Nguyen et al. [45] values owing to a better modeling of the transverse strain effects.
4. The Vo et al. [46] theory consistently noted higher buckling loads than all other methods, particularly for the 1-8-1 scheme.

Table 8 presents the results, which show that the critical buckling loads of thin clamped beams ($l/h = 20$) are generally 1.3–1.4 times higher than those of thick clamped beams ($l/h = 5$). For thin clamped beams, the transverse normal strain effect ($\varepsilon z \neq 0$) results in smaller enhancements than for thick ones, usually 0.7–0.8% as opposed to 5-6% for thick beams. In thin clamped beams, the sandwich beam configurations exhibited smaller but notable variations. With buckling loads of 180.6368 for $k = 0.5$ with $\varepsilon z \neq 0$, the 1-8-1 scheme continues to perform better than the 1-0-1 configuration, which achieves 118.2490, a 53% increase in performance.

The buckling load ratios between successive k values for the 1-0-1 configuration exhibited clear degradation patterns in thin clamped beams. There was a 43.8% decrease from $k = 0$ to $k = 0.5$. demonstrating a 30.1% decrease from $k = 0.5$ to $k = 1$. a 31.4% decrease from $k = 1$ to $k = 2$. There was a 25.3% decrease from $k = 2$ to $k = 5$ and only a 6.2% decrease from $k = 5$ to k = 10. Even in thin beams, the degradation pattern of the 1-8-1 configuration exhibited remarkable stability. There was only a 14.2% decrease from $k = 0$ to $k = 0.5$. There was an 8.0% decrease from $k = 0.5$ to $k = 1$. There was an 8.3% decrease from $k = 1$ to $k = 2$. There was an 8.5% decrease from k=2 to k=5, and only a 3.7% decrease from k=5 to k=10. Even in thin-beam configurations,

Table 7. Nondimensional critical buckling load of C-C FGM sandwich beams with type A for l/h = 5

k	theory	Scheme				
		1-0-1	1-1-1	2-1-2	1-8-1	1-2-1
0	Nguyen et al. [45]	152.1588	152.1588	152.1588	--	152.1588
	Liu et al. [47]	156.9903	154.1932	153.3497	153.1918	154.8889
	Vo et al. [46] $\varepsilon_z \neq 0$	160.2780	160.2780	160.2780	160.2780	160.2780
	Present $\varepsilon_z = 0$	152.1894	152.1894	152.1894	152.1894	152.1894
	Present $\varepsilon_z \neq 0$	160.0357	160.0357	160.0357	160.0357	160.0357
0.5	Nguyen et al. [45]	92.8202	105.6331	99.9361	--	114.1312
	Liu et al. [47]	94.2434	105.9793	101.1266	134.1797	115.3983
	Vo et al. [46] $\varepsilon_z \neq 0$	98.4559	111.9680	105.9750	141.7880	120.8630
	Present $\varepsilon_z = 0$	92.8156	105.6772	99.93997	134.4530	114.2497
	Present $\varepsilon_z \neq 0$	98.3501	111.9417	105.8975	141.8621	120.9212
1	Nguyen et al. [45]	67.5184	83.8267	76.2801	--	95.7230
	Liu et al. [47]	70.2853	85.5390	77.0936	125.3629	97.9329
	Vo et al. [46] $\varepsilon_z \neq 0$	71.7654	89.0834	81.0936	132.5510	101.6130
	Present $\varepsilon_z = 0$	67.3954	83.7873	76.1823	125.5979	95.7985
	Present $\varepsilon_z \neq 0$	71.6677	89.1055	81.0425	132.7607	101.759
2	Nguyen et al. [45]	47.7247	64.4352	56.2259	--	78.5570
	Liu et al. [47]	49.5613	65.9853	57.5994	116.2257	80.5961
	Vo et al. [46] $\varepsilon_z \neq 0$	50.8183	68.6743	59.9354	123.4770	83.6159
	Present $\varepsilon_z = 0$	47.5643	64.3561	56.0900	116.9013	78.6013
	Present $\varepsilon_z \neq 0$	50.6623	68.6768	59.8440	123.7993	83.7844
5	Nguyen et al. [45]	35.5811	49.2949	42.0298	--	63.7847
	Liu et al. [47]	35.7325	50.0061	42.0129	110.2559	65.3243
	Vo et al. [46] $\varepsilon_z \neq 0$	37.8295	52.6395	44.8488	114.7700	68.0510
	Present $\varepsilon_z = 0$	35.3690	49.1641	41.8451	108.5530	63.7732
	Present $\varepsilon_z \neq 0$	37.5736	52.5484	44.6516	115.1689	68.1620
10	Nguyen et al. [45]	32.3345	44.3593	38.0239	--	58.2532
	Liu et al. [47]	31.9495	44.5105	37.1798	106.6613	59.6217
	Vo et al. [46] $\varepsilon_z \neq 0$	34.2824	47.3804	40.5544	111.0120	62.1959
	Present $\varepsilon_z = 0$	32.1193	44.2024	37.8127	104.9853	58.2997
	Present $\varepsilon_z \neq 0$	34.0148	47.2303	40.3015	111.7124	62.2825

the thick-core configuration exhibits superior resistance to changes in material properties, maintaining remarkably consistent degradation rates across all k ranges.

The current studies demonstrate excellent agreement between the theories and configurations. While the ($\varepsilon z \neq 0$) results closely match Vo et al. [46] predictions with discrepancies usually less than 0.2%, the current $\varepsilon z = 0$ results match Nguuyen et al. [45] values within 0.05-0.1%.

Fig. 3 provides a thorough comparison of the buckling behavior under the SS and CC boundary conditions for FGM sandwich beams of Types A and B.

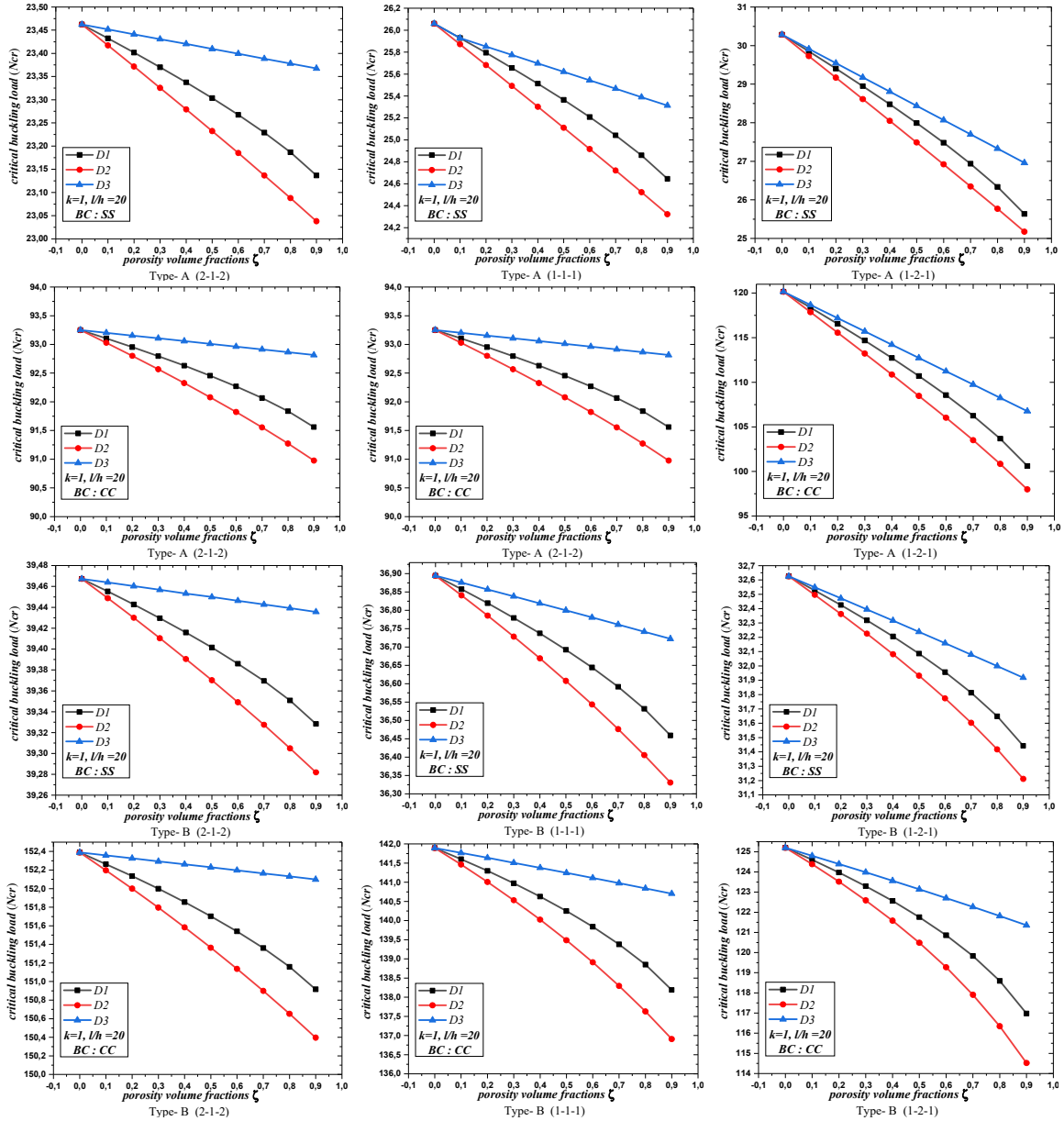

Figure 3. Non-dimensional critical buckling load versus porosity volume fraction of SS and CC sandwich beams for different models

The performances of the three-layer schemes, D1, D2, and D3, differed significantly from each other. In the 2-1-2 configuration, D2 experiences a steep decline of 35-38%, whereas D3 experiences a slight decrease of 8-13% under a 2-1-2 load reduction. At low porosity levels, 2-1-2's symmetrical ceramic-rich outer layers enhance D3, resulting in a 20–25% higher buckling resistance than D2. With a 28–30% decrease, D1 exhibited intermediate behavior. The performance gaps are significantly closed for the 1-1-1 scheme. At high porosities, the initial 12–

Table 8. Nondimensional critical buckling load of C-C FGM sandwich beams with type A for L/h = 20

k	theory	Scheme				
		1-0-1	1-1-1	2-1-2	1-8-1	1-2-1
0	Nguyen et al. [45]	208.9515	208.9515	208.9515	--	208.9515
	Liu et al. [47]	209.9267	210.0771	209.9596	209.9230	210.1792
	Vo et al. [46] $\varepsilon_z \neq 0$	210.7420	210.7420	210.7420	210.7420	210.7420
	Present $\varepsilon_z = 0$	208.9621	208.9621	208.9621	208.9621	208.9621
	Present $\varepsilon_z \neq 0$	210.5324	210.5324	210.5324	210.5324	210.5324
0.5	Nguyen et al. [45]	117.2200	134.4255	126.4422	--	147.0614
	Liu et al. [47]	118.8704	133.1144	127.6891	179.2071	146.2735
	Vo et al. [46] $\varepsilon_z \neq 0$	118.3530	135.6840	127.6410	180.8010	148.4130
	Present $\varepsilon_z = 0$	117.2975	134.4828	126.5054	179.2567	147.1144
	Present $\varepsilon_z \neq 0$	118.2490	135.5730	127.5328	180.6368	148.2961
1	Nguyen et al. [45]	81.9944	102.6655	92.6754	--	119.4215
	Liu et al. [47]	83.0383	103.6351	92.3794	165.6374	120.3777
	Vo et al. [46] $\varepsilon_z \neq 0$	82.7434	103.6060	93.5248	166.4060	120.5090
	Present $\varepsilon_z = 0$	81.9839	102.6630	92.6674	164.9749	119.4304
	Present $\varepsilon_z \neq 0$	82.6762	103.533	93.4540	166.2587	120.4268
2	Nguyen et al. [45]	56.2793	76.1030	65.8505	--	94.9558
	Liu et al. [47]	57.3921	77.2786	65.7944	152.0418	96.1189
	Vo et al. [46] $\varepsilon_z \neq 0$	56.7986	76.8166	66.4664	152.6000	95.8403
	Present $\varepsilon_z = 0$	56.2657	76.0967	65.8393	151.2776	94.9607
	Present $\varepsilon_z \neq 0$	56.7532	76.7773	66.4248	152.4677	95.7916
5	Nguyen et al. [45]	42.0814	56.4973	48.0095	--	74.8903
	Liu et al. [47]	42.6071	57.5360	48.0079	139.3243	76.1057
	Vo et al. [46] $\varepsilon_z \neq 0$	42.4596	57.0343	48.4588	139.6370	75.6019
	Present $\varepsilon_z = 0$	42.0619	56.4868	47.9942	138.4159	74.8899
	Present $\varepsilon_z \neq 0$	42.4049	57.0128	48.4196	139.5203	75.5843
10	Nguyen et al. [45]	39.4962	50.3827	43.3252	--	67.6281
	Liu et al. [47]	39.7863	51.5290	43.5148	134.2185	69.1635
	Vo et al. [46] $\varepsilon_z \neq 0$	39.8436	50.8611	43.7273	134.1223	68.2737
	Present $\varepsilon_z = 0$	39.4763	50.3703	43.3086	133.8981	67.6300
	Present $\varepsilon_z \neq 0$	39.7824	50.8336	43.6765	134.3242	68.2193

15% advantage that D3 has over D2 decreases to just 5-7%. Although D2's shortcomings are somewhat offset by its balanced 1-1-1 architecture, D3 remains consistently superior, by 15–18% on average.

The distribution effects were most significantly amplified in the 1-2-1 configuration. At low porosities, D3 performs 25–28% better than D2, and this difference remains consistent even when the material weakens, with a range of 18–28%. In 1-2-1, the thick ceramic core highlights D2

structural defects while optimizing the benefits of D3 defects. While still in the middle, D1's stable performance profile is more in line with that of D2.

Across all porosity coefficients, the CC configurations of Type A beams exhibited noticeably greater buckling resistance than those of the SS configurations. (CC) beams exhibit a load capacity advantage of roughly 290-300% over the SS beams at ζ=0.2, which progressively diminishes to 250-270% at ζ=0.8. This significant difference resulted from the total rotational restraint of the (CC) beams, which effectively reduced the buckling modes and enhanced the structural stability. Because material weakening dominates over boundary constraints, the performance gap slightly decreases as porosity increases.

Similar trends were observed for Type B beams, although the effects of the boundary conditions were more noticeable. At ζ = 0.2, the (CC) advantage over the SS configurations ranged from 320% to 340%, and at ζ = 0.8, it ranged from 280% to 300%. Because the types of B unique layer architecture affect stress redistribution under constraints, it is more sensitive to boundary conditions, as evidenced by the improved performance.

When (SS) performance of the SS is compared between types, Type A exhibits superior buckling resistance, particularly at lower porosity levels (15–20% higher at ζ = 0.2). At ζ = 0.8, this advantage decreases to 5-8%, demonstrating the relative stability of Type B in high-porosity environments. The crossover points at approximately ζ = 0.6 indicate that as the material integrity declines, the architectural advantages of Type B become increasingly significant.

With performance gains of 18–22%, Type A consistently outperformed Type B for the (CC) configuration at all porosity levels. Because the layer configuration of Type A better withstands the intricate stress distributions caused by clamped supports, this persistent gap demonstrates the inherent structural efficiency of Type A under constrained boundary conditions.

Together, the figures show that the material architecture becomes more significant as the porosity increases, whereas the boundary condition effects predominate at lower porosity levels. Except for the SS configurations at high porosity, Type A typically performs better than Type B, indicating that the best type selection in real-world applications depends on both the expected porosity levels and boundary conditions. The stabilizing effect of clamped boundaries across the porosity range is highlighted by the visual data, which display steeper performance degradation curves for SS systems, in contrast to the more gradual declines in CC systems.

As shown in Fig. 4, the critical buckling loads of the CC beams were significantly higher than those of the SS beams at all l/h ratios, approximately 3.5 to 4.0 times the value.

For type B beams, the pictures in the SS and CC conditions are also very similar, albeit with different magnitudes. The CC beams exhibited better performance once again, as their buckling loads were approximately 3.8-4.2 times higher than those of the SS beams. The slightly greater performance ratio in type B beams implies a greater sensitivity of the different material distributions or core (type B) to the boundary condition effects.

The material-dependent behavior of the SS boundary conditions between type A and type B beams is fascinating. At all ratios of l/h, type B beams have consistently larger critical values of buckling load than type A beams, with the difference being significant at small ratios (in the thick beam region) and gradually decreasing as the ratio increases.

In the case of CC boundary conditions, the comparison between types A and B involves a more complex relationship. Type B retains the buckling loads of type A at higher values, although the increasing consistency with all l/h ratios is greater than in the case of SS. This indicates that the benefits of type B material distribution are enhanced by the clamped end conditions, generating a system of stresses that offers further advantageous utilization of the high strength delivered by this

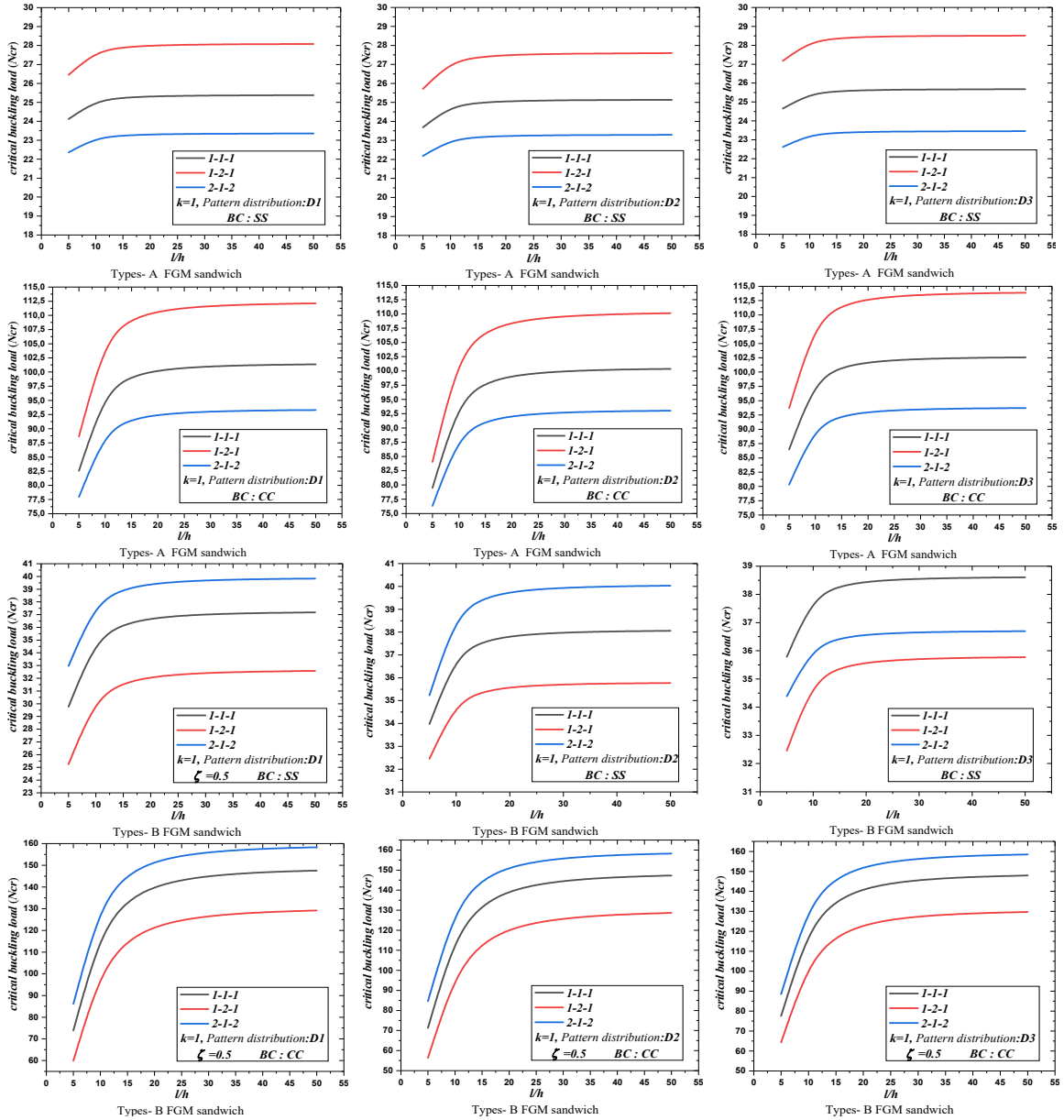

Figure 4. Non-dimensional critical buckling load versus side to thickness ration of SS and CC sandwich beams

arrangement. The rotational restraint at each end resulted in a moment distribution that interacted with the favorable grading pattern of the type B material.

The curves are typical in that the buckling loads rise with the l/h ratio up to a maximum at l/h = 16 in the case of SS beams and l/h = 26 in the case of CC beams, beyond which they tend towards invariance. The critical buckling load in the thick beam zone (low l/h) increases with the slenderness owing to the increase in the flexural rigidity of the beam, which exceeds the increase in length, destabilizing it.

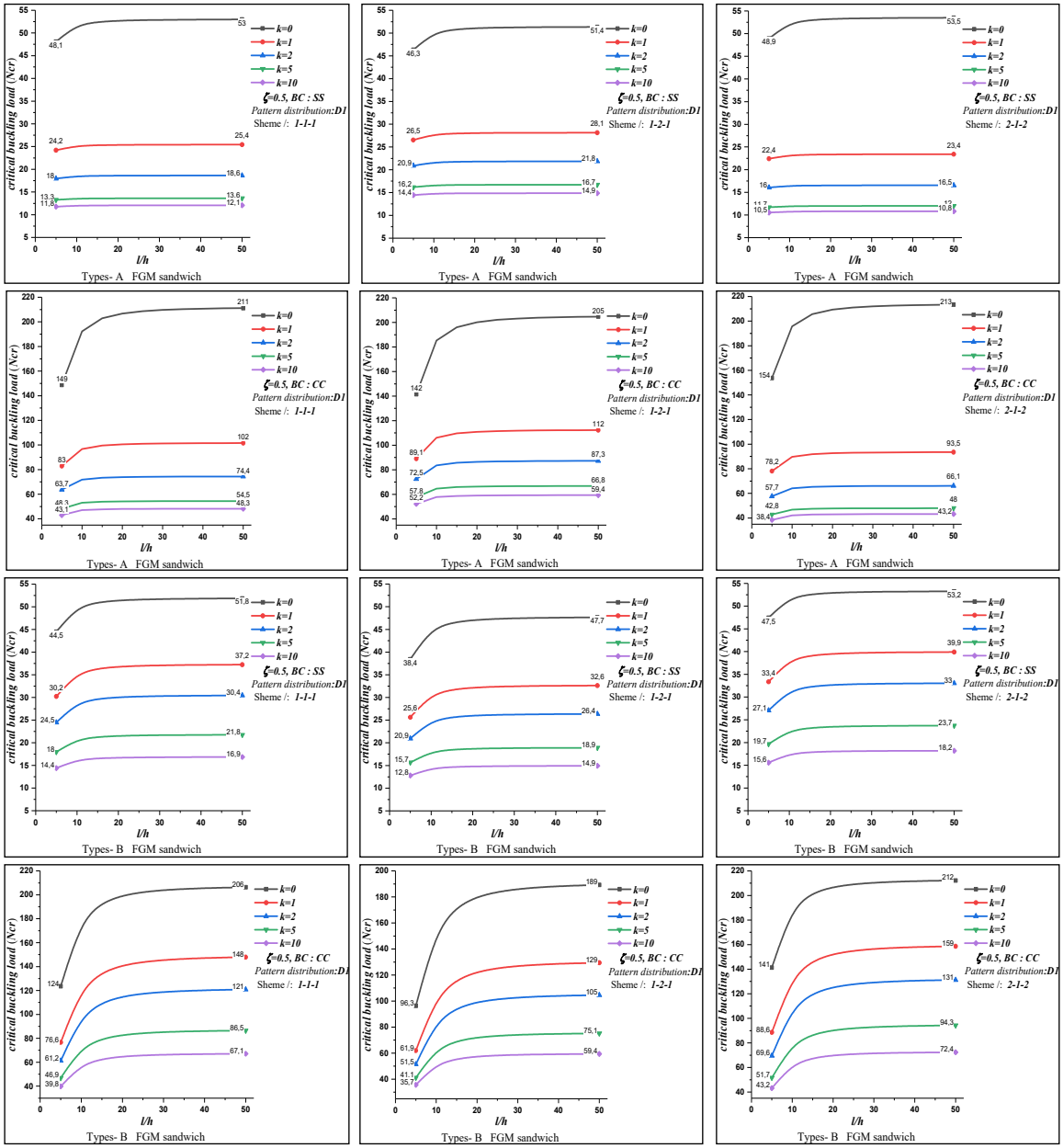

Figure 5. Non-dimensional critical buckling load versus side to thickness ration of SS and CC sandwich beams for different material index

Fig. 5 illustrates the distinct performance characteristics of Type A and Type B (FGM) sandwich beams resulting from the three-layer structures (1-1-1, 1-2-1, and 2-1-2) with varying slenderness ratios (l/h). Under (SS) loads, the Type A loading curves monotonically increased until the critical slenderness ratios were reached: l/h = 15 for Type A and l/h = 12 for Type B, at which point the performance levelled off. The previous plateau of Type B corresponds to its higher

sensitivity to the geometric nonlinearities. The analysis of clamped-clamped (CC) beams revealed greater thresholds (Type A: l/h = 25; Type B: l/h = 20) because the delay in rotation prevented instability.

The 1-1-1 configuration ensures that Type A possesses 15-20 per cent greater buckling resistance than Type B at all l/h ratios because of the better gradation profile that occurs at greater/more useful shear deformation. Above the critical l/h ratios, the performance gap decreased slightly, allowing the global buckling modes to become predominant. In a 1-2-1 beam situation, the amplification is in favor of Type A by 25-30%, and especially at the transition region (l/h = 10-20), stresses across the core-layer interface cause the anticipated premature stiffness loss in Type B. This exhibits the widest divergence, of 30-35%, between Type A and Type B, where the thick ceramic skins serve to resist compressive stresses more effectively, which initiates delamination in Type B.

3. Conclusions

This study investigated the stability response of sandwich beams with functionally graded porosity (FGP) cores and FGM face sheets using virtual work principle and Navier solution. The analytical model was validated against existing literature. Key findings include:

- Clamped-clamped Type A configurations showed superior buckling resistance compared to simply supported configurations across all porosity coefficients.
- For simply supported beams with high porosity, Type A outperformed Type B, demonstrating the importance of considering both porosity levels and boundary conditions in design selection.
- Type B beams consistently exhibited higher critical buckling loads than Type A beams at all side to thickness ratios (l/h).
- Clamped-clamped boundary conditions revealed complex relationships between Type A and Type B performance.
- Critical buckling load increased with slenderness in thick beam zones due to enhanced flexural rigidity.
- The 1-1-1 configuration provided Type A beams with 15-20% greater buckling resistance than Type B across all side to thickness ratios (l/h).
- Thick ceramic skins effectively resisted compressive stress.

These findings provide engineering guidelines for designing sandwich beams with optimized dynamic characteristics and stability performance based on specific application requirements.

References

References

1. Belarbi, M.O., Karamanli, A., Benounas, S., Daikh, A.A. (2025). Bending, free vibration and buckling finite element analysis of porous functionally graded plates with various porosity distributions using an improved FSDT. Mechanics Based Design of Structures and Machines, 53(1), 401-445. https://doi.org/10.1080/15397734.2024.2366530.

2. Mohamed, I., Kahya, V., Şimşek, S. (2025). A new higher-order finite element model for free vibration and buckling of functionally graded sandwich beams with porous core resting on a two-parameter elastic foundation using quasi-3D theory. Iranian Journal of Science and Technology, Transactions of Civil Engineering, 49(1), 383-408. https://doi.org/10.1007/s40996-024-01482-x.
3. Turan, M., Adiyaman, G. (2024). Free vibration and buckling analysis of porous two-directional functionally graded beams using a higher-order finite element model. Journal of Vibration Engineering & Technologies, 12(1), 1133-1152. https://doi.org/10.1007/s42417-023-00898-5.
4. Chintalapudi, R., Narayanan Kannaiyan, G., Pappula, B., Makgato, S. (2024). The effects of gradient index, aspect ratio, porosity, and boundary conditions on the buckling behavior of functionally graded porous beams: A k-out-of-n system reliability analysis. Results in Physics, 60, 107634. https://doi.org/https://doi.org/10.1016/j.rinp.2024.107634.
5. Akgöz, B., Civalek, Ö. (2022). Buckling analysis of functionally graded tapered microbeams via Rayleigh–Ritz method. Mathematics, 10(23), 4429. https://doi.org/https://doi.org/10.3390/math10234429.
6. Bridjesh, P., Geetha, N., Yelamasetti, B. (2024). Numerical investigation on buckling of two-directional porous functionally graded beam using higher order shear deformation theory. International Journal on Interactive Design and Manufacturing (IJIDeM), 18(5), 2805-2818. https://doi.org/10.1007/s12008-023-01332-6.
7. Geetha, N., Reddy, G., Bridjesh, P. (2023). Higher order shear deformation theory for functionally graded porous beam-numerical free vibrational analysis. Journal of Engineering Science & Technology Review, 16(5). https://doi.org/10.25103/jestr.165.08.
8. Nguyen, N.D., Nguyen, T.N., Nguyen, T.K., Vo, T.P. (2022). A new two-variable shear deformation theory for bending, free vibration and buckling analysis of functionally graded porous beams. Composite Structures, 282, 115095. https://doi.org/10.1016/j.compstruct.2021.115095.
9. Chitour, M., Bouhadra, A., Benguediab, M., Mansouri, K., Menasria, A., Tounsi, A. (2022). A new high order theory for buckling temperature analysis of functionally graded sandwich plates resting on elastic foundations. https://doi.org/10.21272/jnep.14(3).03028.
10. Tamrabet, A., Mamen, B., Menasria, A., Bouhadra, A., Tounsi, A., Ghazwani, M.H., Alnujaie, A., Mahmoud, S. (2023). Buckling behaviors of FG porous sandwich plates with metallic foam cores resting on elastic foundation. Structural Engineering and Mechanics, 85(3), 289-304. https://doi.org/10.12989/sem.2023.85.3.289.
11. Berkia, A., Benguediab, S., Menasria, A., Bouhadra, A., Bourada, F., Mamen, B., Tounsi, A., Benrahou, K. H., Benguediab, M., Hussain, M. (2022). Static buckling analysis of bi-directional functionally graded sandwich (BFGSW) beams with two different boundary conditions. Steel and Composite Structures, 44(4), 503-517. https://doi.org/10.12989/scs.2022.44.4.503.
12. Messaoudi, A., Bouhadra, A., Menasria, A., Mamen, B., Boucham, B., Benguediab, M., Tounsi, A., Al-Osta, M. (2023). Impact of the shear and thickness stretching effects on the free vibrations of advanced composite plates. Mechanics of Composite Materials, 59(5), 1001-1018. https://doi.org/10.1007/s11029-023-10148-0.
13. Slimani, R., Menasria, A., Ali Rachedi, M., Mourad, C., Refrafi, S., Nimer, A.A., Bouhadra, A., Mamen, B. (2024). A novel quasi-3D refined HSDT for static bending analysis of porous functionally graded Plates. Journal of Computational Applied Mechanics, 55(3), 519-537. https://doi.org/10.22059/jcamech.2024.372417.968.
14. Tamrabet, A., Mourad, C., Ali Alselami, N., Menasria, A., Mamen, B., Bouhadra, A. (2024). Efficient kinematic model for stability analysis of imperfect functionally graded sandwich plates with ceramic middle layer and varied boundary edges. Journal of Computational Applied Mechanics, 55(2), 184-200. https://doi.org/10.22059/jcamech.2024.371464.947.
15. Van Do, T., Hong Doan, D., Chi Tho, N., Dinh Duc, N. (2022). Thermal buckling analysis of cracked functionally graded plates. International Journal of Structural Stability and Dynamics, 22(8), 2250089. https://doi.org/10.1142/S0219455422500894.

16. Nguyen, N.D., Bui, V.T., Nguyen, T.K. (2024). A modified strain gradient theory for buckling, bending and free vibration behaviors of metal foam microbeams. Structures, https://doi.org/10.1016/j.istruc.2024.106533.
17. Chen, D., Rezaei, S., Rosendahl, P.L., Xu, B.X., Schneider, J. (2022). Multiscale modelling of functionally graded porous beams: Buckling and vibration analyses. Engineering Structures, 266, 114568. https://doi.org/10.1016/j.engstruct.2022.114568.
18. Wang, S., Ding, W., Li, Z., Xu, B., Zhai, C., Kang, W., Yang, W., Li, Y. (2023). A size-dependent quasi-3D model for bending and buckling of porous functionally graded curved nanobeam. International Journal of Engineering Science, 193, 103962. https://doi.org/10.1016/j.ijengsci.2023.103962.
19. Karamanli, A., Vo, T.P. (2021). Bending, vibration, buckling analysis of bi-directional FG porous microbeams with a variable material length scale parameter. Applied Mathematical Modelling, 91, 723-748. https://doi.org/10.1016/j.apm.2020.09.058.
20. Khatir, B., Filali, S., Belabdeli, S., Daikh, A.A., Khatir, S., Capozucca, R., Cuong-Le, T. (2024). Vibration analysis of new cosine functionally graded microplates using isogeometric analysis. Structures, https://doi.org/10.1016/j.istruc.2024.107467.
21. Adiyaman, G., Turan, M. (2024). Bending and buckling analysis of porous 2D functionally graded beams with exponential material property variation. Iranian Journal of Science and Technology, Transactions of Civil Engineering, 1-28. https://doi.org/10.1007/s40996-024-01508-4.
22. Wu, S., Li, Y., Bao, Y., Zhu, J., Wu, H. (2024). Examination of beam theories for buckling and free vibration of functionally graded porous beams. Materials, 17(13), 3080. https://doi.org/10.3390/ma17133080.
23. Nguyen, Q.K., Nguyen, N.D. (2024). Legendre–Ritz solution for free vibration and buckling analysis of porous microbeams. Journal of Vibration Engineering & Technologies, 12(3), 4747-4764. https://doi.org/10.1007/s42417-023-01148-4.
24. Nguyen, N., Nguyen, T. (2024). Chebyshev polynomial-based Ritz method for thermal buckling and free vibration behaviors of metal foam beams. Applied Mathematics and Mechanics, 45(5), 891-910. https://doi.org/10.1007/s10483-024-3116-5.
25. Turan, M., Uzun Yaylacı, E., Yaylacı, M. (2023). Free vibration and buckling of functionally graded porous beams using analytical, finite element, and artificial neural network methods. Archive of Applied Mechanics, 93(4), 1351-1372. https://doi.org/10.1007/s00419-022-02332-w.
26. Belarbi, M.O., Daikh, A.A., Garg, A., Hirane, H., Houari, M.S.A., Civalek, Ö., Chalak, H. (2022). Bending and free vibration analysis of porous functionally graded sandwich plate with various porosity distributions using an extended layerwise theory. Archives of Civil and Mechanical Engineering, 23(1), 15. https://doi.org/10.1007/s43452-022-00551-0.
27. Le, Q.C., Nguyen, B.D. (2023). Analysis of the free vibration of porous functionally graded beams with different boundary conditions and a novel two-variable model. Proceedings of the 2023 8th International Scientific Conference on Applying New Technology in Green Buildings (ATiGB), https://doi.org/10.1109/ATiGB59969.2023.10364425.
28. Gaspar, J., Loja, M., Barbosa, J. (2023). Static and free vibration analyses of functionally graded plane structures. Journal of Composites Science, 7(9), 377. https://doi.org/10.3390/jcs7090377.
29. Gawah, Q., Al-Osta, M.A., Abdullah, M.A., Bourada, F., Tounsi, A., Ahmad, S., Al-Dulaijan, S.U., Al-Zahrani, M.M. (2025). Wave propagation analysis of graphene platelet-reinforced functionally graded porous plates resting on viscoelastic foundations using an integral HSDT. Thin-Walled Structures, 215, 113502. https://doi.org/10.1016/j.tws.2025.113502.
30. Daouadji, B.H., Attia, A., Bousahla, A.A., Tounsi, A., Tounsi, A., Mohamed, S.M., Althobaiti, S., Selim, M.M., Yaylaci, M., Aldosari, S.M. (2025). On the bending behavior of porous functionally graded plates under hygrothermo-mechanical loads. Geomechanics and Engineering, 42(3), 191-206. https://doi.org/10.12989/gae.2025.42.3.191.
31. Benchohra, M., Laoufi, I., Attia, A., Bousahla, A.A., Tounsi, A., Tounsi, A., Yaylaci, M., Alluqmani, A. E., Mahmoud, S. (2025). Analytical solution for imperfect functionally graded beams resting on

viscoelastic foundation. Structural Engineering and Mechanics, 95(2), 155-167. https://doi.org/10.12989/sem.2025.95.2.155.

32. Rajeh, M.A., Al-Dulaijan, S.U., Bourada, F., Al-Osta, M.A., Tounsi, A., Yaylacı, M., Tounsi, A. (2025). On the thermal bending behavior of porous cross-ply laminated plates using an improved first-order shear deformation theory. Acta Mechanica, 1-19. https://doi.org/10.1007/s00707-025-04369-8.
33. Tounsi, A., Kaci, A., Tounsi, A., Al-Osta, M.A., Yaylacı, M., Mohamed, S.M., Althobaiti, S., Selim, M. M. (2025). Quasi-3D plate theory for size-dependent static and free vibration analysis of FG microplate with porosities based on a modified couple stress theory. Mechanics of Advanced Materials and Structures, 1-24. https://doi.org/10.1080/15376494.2025.2463687.
34. Kaddari, M., Balubaid, M., Mahmoud, S., Kaci, A., Bousahla, A.A., Tounsi, A., Al-Osta, M.A., Tounsi, A. (2025). Influence of porosity distribution on buckling behavior of FG sandwich plates using a quasi-3D refined plate theory. Mechanics Based Design of Structures and Machines, 53(5), 3635-3662. https://doi.org/10.1080/15397734.2024.2434552.
35. Tounsi, A., Belabed, Z., Bounouara, F., Balubaid, M., Mahmoud, S., Bousahla, A.A., Tounsi, A. (2024). A finite element approach for forced dynamical responses of porous FG nanocomposite beams resting on viscoelastic foundations. International Journal of Structural Stability and Dynamics, 2650078. https://doi.org/10.1142/S0219455426500781.
36. Driz, H., Attia, A., Bousahla, A.A., Addou, F.Y., Bourada, M., Tounsi, A., Tounsi, A., Balubaid, M., Mahmoud, S. (2024). Dynamic response of imperfect functionally graded plates: impact of graded patterns and viscoelastic foundation. Structural Engineering and Mechanics, 91(6), 551-565. https://doi.org/10.12989/sem.2024.91.6.551 .
37. Alsubaie, A.M., Al-Osta, M.A., Alfaqih, I., Tounsi, A., Chikh, A., Mudhaffar, I.M., Al-Dulaijan, S.U., Tahir, S. (2024). Influences of porosity distributions on bending and buckling behaviour of functionally graded carbon nanotube-reinforced composite beam. Computers and Concrete, 34(2), 179-193. https://doi.org/10.12989/cac.2024.34.2.179.
38. Al-Houri, S., Al-Osta, M.A., Bourada, F., Gawah, Q., Tounsi, A., Al-Dulaijan, S.U. (2025). Analysis of porosity-dependent wave propagation in FG-CNTRC beams utilizing an integral higher-order shear deformation theory. International Journal of Structural Stability and Dynamics, 25(22), 2550233. https://doi.org/10.1142/S0219455425502335.
39. Tounsi, A., Tahir, S.I., Al-Osta, M.A., Do-Van, T., Bourada, F., Bousahla, A.A., Tounsi, A. (2023). An integral quasi-3D computational model for the hygro-thermal wave propagation of imperfect FGM sandwich plates. Computers and Concrete, 32(1), 61-74. https://doi.org/10.12989/cac.2023.32.1.061.
40. Bentrar, H., Chorfi, S.M., Belalia, S.A., Tounsi, A., Ghazwani, M.H., Alnujaie, A. (2023). Effect of porosity distribution on free vibration of functionally graded sandwich plate using the P-version of the finite element method. Structural Engineering and Mechanics, 88(6), 551-567. https://doi.org/10.12989/sem.2023.88.6.551.
41. Addou, F.Y., Bourada, F., Meradjah, M., Bousahla, A.A., Tounsi, A., Ghazwani, M.H., Alnujaie, A. (2023). Impact of porosity distribution on static behavior of functionally graded plates using a simple quasi-3D HSDT. Computers and Concrete, 32(1), 87-97. https://doi.org/10.12989/cac.2023.32.1.087.
42. Alsubaie, A.M., Alfaqih, I., Al-Osta, M.A., Tounsi, A., Chikh, A., Mudhaffar, I.M., Tahir, S. (2023). Porosity-dependent vibration investigation of functionally graded carbon nanotube-reinforced composite beam. Computers and Concrete, 32(1), 75-85. https://doi.org/10.12989/cac.2023.32.1.075.
43. Chen, D., Yang, J., Kitipornchai, S. (2015). Elastic buckling and static bending of shear deformable functionally graded porous beam. Composite Structures, 133, 54-61. https://doi.org/10.1016/j.compstruct.2015.07.052.
44. Jamshidi, M., Arghavani, J. (2018). Optimal material tailoring of functionally graded porous beams for buckling and free vibration behaviors. Mechanics Research Communications, 88, 19-24. https://doi.org/10.1016/j.mechrescom.2018.01.006.
45. Nguyen, T.K., Nguyen, B.D. (2015). A new higher-order shear deformation theory for static, buckling and free vibration analysis of functionally graded sandwich beams. Journal of Sandwich Structures & Materials, 17(6), 613-631. https://doi.org/10.1177/1099636215589237.

46. Vo, T.P., Thai, H.T., Nguyen, T.K., Inam, F., Lee, J. (2015). A quasi-3D theory for vibration and buckling of functionally graded sandwich beams. Composite Structures, 119, 1-12. https://doi.org/10.1016/j.compstruct.2014.08.006.
47. Liu, J., He, B., Ye, W., Yang, F. (2021). High performance model for buckling of functionally graded sandwich beams using a new semi-analytical method. Composite Structures, 262, 113614. https://doi.org/10.1016/j.compstruct.2021.113614.